LJMU Research Online

Joksimovic, M, Levi, E and Vukosavic, S

 Near-complete suppression of harmonic currents in SPMSMs caused by back emf and dead time

http://researchonline.ljmu.ac.uk/id/eprint/17175/

Article

For more information please contact researchonline@ljmu.ac.uk

Near-complete suppression of harmonic currents in SPMSMs caused by back emf and dead time

Miodrag Joksimovic, *Student Member, IEEE*, Emil Levi, *Fellow, IEEE*, Slobodan Vukosavic, *Senior Member, IEEE*

Abstract—This paper introduces a novel algorithm forsuppression of phase current harmonics in three-phase sinusoidal surface mounted permanent magnet synchronous machines (SPMSMs) caused by non-ideal back-emf waveform and dead-time effects. Proposed feedback acquisition chain obtains an exact information on all the relevant harmonics within each period of the fundamental. Design of the harmonic current controller based on the internal model control principle is given. The paper outlines the relevant details of implementation and the results of verification performed by both computer simulations and experimentally, using a laboratory prototype machine. Experimental results, obtained in presence of non-sinusoidal back-emf and with erroneous dead-time compensation, prove the ability of the proposed solution to remove the stator current harmonics quickly, in just two fundamental periods, and thus eliminate torque ripple.

Index Terms—SPMSM, adaptive control, harmonic compensation, dead-time compensation.

I. INTRODUCTION

SURFACE permanent magnet synchronous machines are used in various industrial applications, ranging from appliance-grade to high-end [1], [2], [3]. In order to achieve high power density, the machines are often designed in a way that gives rise to considerable back-emf harmonics (brushless dc motors, BLDC). Such designs come with a large torque ripple, which is a shortcoming that limits their use in high-bandwidth applications. The main electrical factor that causes the torque ripple is current harmonics, which depend on control technique, dead time of the inverter, and back-emf harmonics [4].

Various attempts to remove the torque ripple in steady state and during transients have been made. Solutions reported in [5] - [6] consider drives with commutation scheme which contributes to reduction of the torque ripple down to 5% - 8%. A dc-link voltage modulation circuit to temporarily increase dc-link voltage in the current commutation period is introduced in [7], resulting in torque ripple of 7.75% at high, and 6% at low speeds.

Solutions reported in [8] and [6] propose modification of the dc-link circuit and reduce commutation-related torque ripple down to 5%. A method presented in [9] uses a spider based controller, and reports a torque ripple of 7%. In [10], the authors prove that the torque ripple could be considerably lower in motors with sinusoidal phase currents provided that the current waveforms are free from harmonic distortions.The motors can also be designed for operation with sinusoidal currents, in which case they are called sinusoidal permanent magnet synchronous machines (SPMSMs).

Comparative study of sinusoidal vs square-wave current supply of the PM machine with square wave back-emf [11] shows that the sinusoidal current supply outperforms the real square-wave current supply across almost entire speed range. Indeed, the torque-speed characteristic is higher, especially when approaching the base speed, and the torque ripple is lower, apart from a narrow speed interval centered at half of the nominal speed.

Most permanent magnet drives with sinusoidal currents and fast torque response adopt Field Oriented Control (FOC), which is commonly achieved with synchronous frame controllers having the current loop bandwidth $f_{bw} > 1$ kHz [12]. When the back-emf is non-sinusoidal, most relevant harmonics are at frequencies well beyond the bandwidth frequency f_{bw}, and the current controller cannot suppress the stator current content at frequencies of such harmonics [13].

The machine used in this work is a cheaper version of the SPMSM, such that the back-emf spectrum does possess higher harmonics, as in a BLDC machine. However, the values of these harmonics are insufficient to enable effective torque enhancement by higher order stator current harmonic injection, as will be shown later on. Hence the machine is controlled to produce only the fundamental torque component, requiring full suppression of the stator current harmonics.

The combination of back-emf harmonics [14] and relatively low phase impedance gives rise to non-negligible amplitudes of undesired phase current harmonics, which cause acoustic noise and the torque ripple [1], [15]. If these harmonics remain unaccounted for, the drive is not suitable for applications with strict requirements on vibrations, torque ripple and noise. Numerous efforts have therefore already been directed toward reduction and/or minimization of the torque ripple in the SPMSMs. A frequently studied approach [16], [17], [18] is based on the use of principles of repetitive control. Artificial-intelligence-based techniques, such as fuzzy logic control [19] and genetic algorithms [20] have also been applied to the problem of torque ripple minimization. Further notable and interesting examples include use of sliding mode control [21], iterative learning control [22], as well as a multiple reference frame approach [23], dedicated modelling techniques [24], and even a torque meter [25].

This paper proposes a novel algorithm for suppression of higher harmonic currents, arising from both the back-emf and dead time, by means of a novel harmonic-suppression controller. Phase currents are sampled, processed in the pre-scribed manner, and passed on to harmonic current controllers, each implemented in a corresponding frame of reference, which give voltage commands required to suppress current

harmonics.

The paper is organised as follows. Proposed feedback acquisition chain which outputs the relevant stator current harmonics in each period of the fundamental is presented in section II. The structure and parameter setting of harmonic suppression controllers are given in section III. Simulation results are presented in section IV, with a subsequent full experimental verification provided in section V. Section VI provides the conclusions of this paper.

II. FEEDBACK ACQUISITION CHAIN

Efficient suppression of back-emf caused current harmonics requires their quick and accurate detection from the stator currents, which in turn calls for precise current measurement. Proposed approach relies on oversampling and PWM averaging [26], followed by extraction of individual harmonics by one-fundamental-period averaging in multiple reference frames [15].

A. One-Fundamental-Period Averaging

The amplitude and frequency of back-emf harmonics change with the rotor angular velocity. Compared to the time constant of a high-bandwidth current regulator, such changes are relatively slow. One can then assume that the current harmonics arising from the non-sinusoidal back-emf are almost constant during one period of the fundamental frequency. Without the loss of generality, it can be assumed that the phase currents I_{abc} have the fundamental, the 5th and the 7th harmonic components:

$$I_a = A_1 sin(\omega_e t + \phi_1) + A_5 sin(-5\omega_e t + \phi_5) +$$
$$+ A_7 sin(7\omega_e t + \phi_7). \tag{1}$$

The minus sign in the fifth harmonic indicates negative sequence. Transformation to the synchronous reference frame (SRF) requires Clarke's and Park's transformation with $\theta_e = +\omega_e t$ and provides I_{dq} currents. Using complex notation, I_{dq} is

$$I_{dq} = I_d + j \cdot I_q = A_1 e^{j\phi_1} + A_5 e^{j(-6\omega_e t + \phi_5)} + A_7 e^{j(6\omega_e t + \phi_7)}, \tag{2}$$

where A_1, A_5, A_7 and ϕ_1, ϕ_5, ϕ_7 are amplitudes and phases of the first, the fifth and the seventh harmonic components, respectively, and ω_e is the fundamental electrical angular frequency of the machine. Applying Park's transformation with $\theta_{6e} = -6\omega_e t$ on the I_{dq}, one would acquire the currents in the 5th harmonic synchronous frame

$$I_{dq}^5 = I_{dq} \cdot e^{j6\omega_e t}$$
$$= A_1 e^{j(6\omega_e t + \phi_1)} + A_5 e^{j\phi_5} + A_7 e^{j(12\omega_e t + \phi_7)}. \tag{3}$$

The A_5 component of the stator current (3) is obtained by considering the average value obtained within one period of the fundamental,

$$\overline{I_{dq}^5} = \overline{I_d^5} + j \cdot \overline{I_q^5} = \frac{1}{T_e} \int_0^{T_e} I_{dq}^5 \; dt = A_5 \cdot e^{j\phi_5}. \tag{4}$$

Assuming that the rotor speed does not change over one fundamental period, dt is replaced by $d(\theta_e/\omega_e)$ to obtain

$$\overline{I_{dq}^5} = \frac{1}{2\pi} \int_0^{2\pi} I_{dq}^5 \; d\theta_e = A_5 \cdot e^{j\phi_5}. \tag{5}$$

Thus, if the current I_{dq}^5 is integrated and the integrator is reset at each zero-crossing of the angle θ_e, the integrator output captured prior to the reset will provide the information on A_5
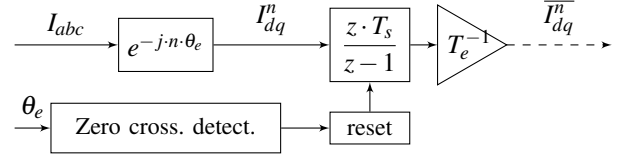

Fig. 1: Principle of measuring the nth current harmonic.

and ϕ_5. A block diagram of the described method is given in Fig. 1. Using the same reasoning, it is possible to extract the amplitude and phase of all the relevant harmonics.

It has to be noted that, in a special case, when the phase current harmonic spectrum does not have triplen harmonics, or in a case when phase current spectrum comprises only odd harmonics (without triplen), it is possible (but not used here) to accelerate the feedback acquisition path by averaging on a smaller period $T_{avg} = T_{fund}/3$ or $T_{avg} = T_{fund}/6$, respectively.

Proposed harmonic extraction relies on the fundamental period of the output voltage. Provided with an exact electrical period, and with proposed oversampling-and-averaging based signal processing, proposed harmonic detection does not get affected by the voltage saturation.

B. Suppressing the Impact of Drive Transients

The presented method of current harmonic measurement relies on the fact that the integral of a sinusoidal function over its period is equal to zero. However, in practical implementations, the amplitude of the fundamental current constantly changes, since the flux and torque controllers permanently alter I_d^{ref} and I_q^{ref} current references, the latter being related to the output of the speed or position controller. Permanent changes of I_{dq}^{ref} affect the amplitude of fundamental currents, which affect the measurement of relevant harmonics. The worst case scenario would be the one in which the amplitude of the fundamental changes at one half of the fundamental period. In this case, the average value of the fundamental, seen from the harmonic frame of reference, would differ from zero, and would give false measurement of harmonic current. This "false measurement" would then excite the harmonic current controller which would generate unnecessary voltage commands in an attempt to suppress non-existent harmonics, thus impairing the torque response and the drive performance. This phenomenon has to be dealt with.

If the fundamental components were known in advance, it could be possible to remove their impact on the harmonic feedback. With the references I_d^{ref} and I_q^{ref} of the fundamental currents, the actual currents could be derived from known transfer function of the digital current controller. The obtained estimates would correspond to the stator currents obtained in hypothetical case where the back-emf and dead-time disturbances are negligible. The closed-loop transfer function $W_{CC}^e(z) = I_{dq}(z)/I_{dq}^{ref}(z)$ depends on the load transfer function W_L^e, fundamental current controller transfer function W_{REG}^e and the transfer function of the feedback acquisition chain W_{FB} (these are shown in Fig. 2). Required transfer functions are derived in Appendix A. With direct-path transfer function W_{OL}^e of (6), the closed-loop transfer function is given in (7).

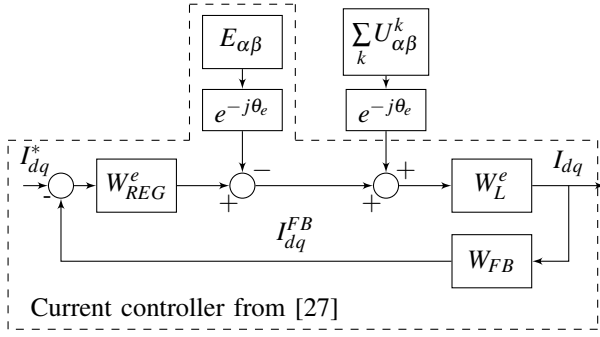$$W_{OL}^e = W_{REG}^e \cdot W_L^e = \frac{\alpha_d}{z - 1} \tag{6}$$

Fig. 2: Block diagram of fundamental current regulator, in the synchronous reference frame [27].
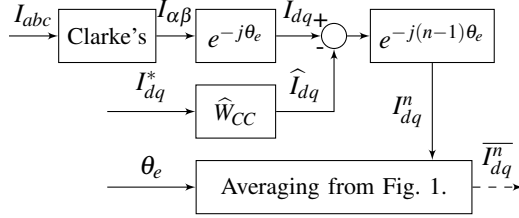

Fig. 3: Block diagram of harmonic acquisition path free from fundamental current transients.

$$W_{CC}^e = \frac{I_{dq}}{I_{dq}^{ref}} = \frac{W_{OL}^e}{1 + W_{OL}^e \cdot W_{FB}} = \frac{2 \cdot \alpha_d \cdot z}{2 \cdot z^2 + (\alpha_d - 2) \cdot z + \alpha_d}, \quad (7)$$

Parameter α_d is an adjustable gain. Transfer function (7) can be used to create an estimator of undisturbed I_{dq} currents,

$$\widehat{I}_{dq} = \widehat{W}_{CC}^e \cdot I_{dq}^{ref}. \quad (8)$$

Estimated values of $\widehat{I}_{dq}$ currents are subtracted from measured I_{dq} currents to create a signal free from I_{dq} transients, comprising only current components arising from higher harmonics. This signal is transformed into corresponding reference frame and averaged over one fundamental period, as shown in Fig. 3. Number n in the second Park's transformation in Fig. 3 has an algebraic value corresponding to the relevant harmonic's order and sequence (positive or negative).

III. HARMONIC COMPENSATION

With the prescribed feedback acquisition chain, the sampling frequency is inherently set to the frequency of the fundamental. In practice, it is variable and it can not exceed a couple of hundreds of Hz. This sampling rate is considerably lower than the one used in conjunction with conventional digital current controllers. Therefore, the plant transfer function as seen by the harmonic suppression controller is considerably different from the plant transfer function seen by the conventional digital current controller. In order to design a harmonic controller, one must get an insight into the behaviour of current controlled machine enhanced by the proposed feedback acquisition chain, in order to derive the plant transfer function required for the proper design of the harmonic controller. After the individual harmonic controller's structure and parameters are obtained, the harmonic suppression system shall be obtained by parallel operation of m harmonic controllers, as shown in Fig. 4.

A. Fundamental Controller

Harmonic controllers will be designed to work in conjunction with a fundamental current controller (FCC), which controls torque and flux of the machine, by controlling the direct and quadrature currents. This paper relies on the decoupling FCC presented in [26], with one-PWM-period feedback averaging and with advanced scheduling of control tasks. However, it is important to note that the following reasoning applies to any fundamental current controller, as long as its closed-loop transfer function is known. Discrete domain transfer function of FCC which this paper relies on, is [27]

$$W_{REG}(z) = \frac{U_{dq}}{I_{dq}} = \frac{\alpha_d L_s}{T_S} \cdot \frac{z \cdot e^{-j\omega_e T_S} - e^{-\beta}}{z - 1}, \quad (9)$$

where T_S is sampling period, R_s and L_s are phase resistance and inductance of the machine and $\beta = R_s \cdot T_S / L_s$. The complex notation implies coupling of d and q axes. With $\alpha_d = 0.20$, this regulator provides a fast response with overshoot of 0% and bandwidth $f_{bw}(-3db) = 0.0497 \cdot f_s$, $f_s = 2 \cdot f_{pwm}$ being the sampling frequency, and exhibits stable behaviour with vector margin of 0.6917. Block diagram of this FCC is given in Fig. 2.

In Fig. 2, the block diagram taken from [27] is delimited by the dashed-line box. Within this box, $E_{\alpha\beta}$ represents the electromotive force of the controlled motor, acting as the voltage disturbance. Sum of external voltage signals $U_{\alpha\beta}^k$, $k \in [5, 7, 11, 13, 17, 19]$, k being the harmonic number of any relevant harmonic, is added to the voltage command $U_{\alpha\beta}$ in order to suppress the current harmonics. The signals $U_{\alpha\beta}^k$ are obtained from individual harmonic controllers.

Low-pass nature of the motor and reduced amplitudes of higher-order back-emf harmonics contribute to a significant reduction in amplitude of the corresponding higher-order current harmonics. Therefore, it is reasonable to assume that the harmonics to be taken care of are the 5th and 7th, accompanied in most cases with the 11th and 13th, with rarely any need to consider higher order harmonics.

A brief example which illustrates how the order of higher emf harmonic affects the amplitude of higher current harmonic follows. From experimental recording, reported later in Section IV, the ratio of 17th to 5th harmonic amplitude $E_{17}/E_5 \approx 1/3$ can be obtained. For a high enough fundamental frequency, the amplitude of currents arising from these harmonics will dominantly be limited by phase impedance of the machine $R_s + j \cdot \omega_x L_s$, $\omega_x = n \cdot \omega_e$ being the angular frequency of the given harmonic

$$\frac{I_{17}}{I_5} = \frac{1/\sqrt{R^2 + (17 \cdot \omega_e \cdot L)^2}}{1/\sqrt{R^2 + (5 \cdot \omega_e \cdot L)^2}} \cdot \frac{E_{17}}{E_5}. \quad (10)$$

At high enough angular frequency, phase resistance becomes an order of magnitude lower than the reactance $R << X_L = \omega_e \cdot L_s$. Approximating (10) gives

$$\frac{I_{17}}{I_5} = \frac{\sqrt{(5 \cdot \omega_e \cdot L)^2}}{\sqrt{(17 \cdot \omega_e \cdot L)^2}} \cdot \frac{E_{17}}{E_5} = \frac{5}{17} \cdot \frac{1}{3} = 0.098. \quad (11)$$

B. Transfer Function of Equivalent Load

Design of the harmonic suppression controller starts with the plant transfer function, namely, the function that relates the stator current harmonics, as an output, to the back-emf harmonic disturbance as an input. Such transfer function is obtained from disturbance transfer function $Y^e(z)$ of [27], relating the voltage disturbance to the output current. With
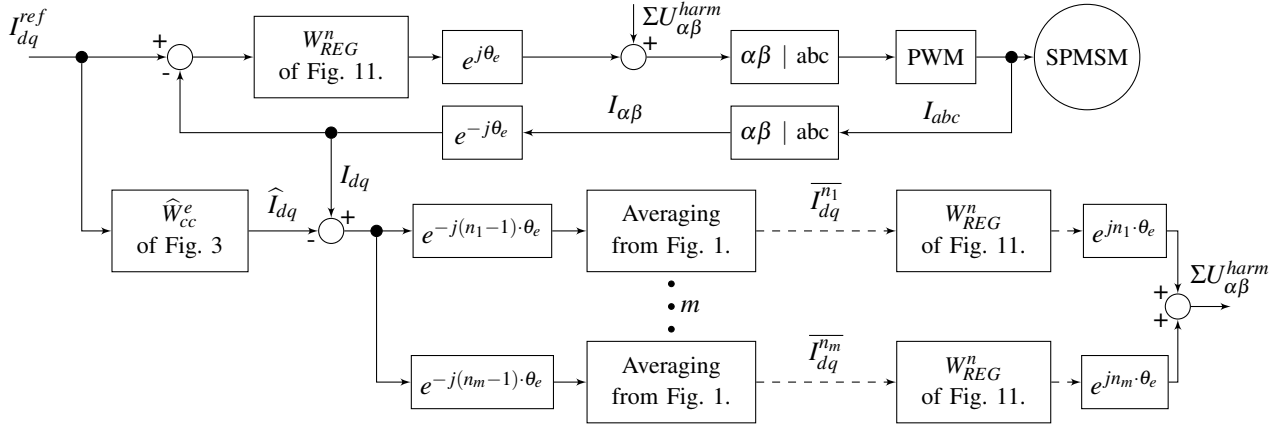
Fig. 4: Block diagram of the current controlled SPMSM drive enhanced with harmonic current controllers. Lower part of the diagram depicts m harmonic current controllers, which constitute harmonic suppressor, working simultaneously. Solid and dashed lines represent signals with sample rate f_s and f_e respectively.

one-fundamental-period averaging in the feedback chain, the sampling time of harmonic controllers is equal to one period of the fundamental. With settling time of contemporary current controllers [12] several tens of times shorter, a transient caused by the harmonic controller output would settle rather quickly. Therefore, it is reasonable to consider the steady state values of disturbance transfer function $Y^e(j\omega_e)$.

The equivalent load transfer function will be found by analysing the disturbance transfer function of the closed-loop system given in Fig. 2.

The transfer function of the machine in the discrete time domain and synchronous frame of reference is [12]

$$W_L^e(z) = \frac{T_S}{L} \cdot \frac{1}{z \cdot e^{-j\omega_e T_S} - e^{-\beta}}, \tag{12}$$

and the transfer function of the controller is given in (9). With principles of one-PWM-period averaging of the feedback path, and the advanced scheduling of control tasks [26], [27], and assuming $f_s = f_{pwm}$, the feedback transfer function is

$$W_{FB}(z) = \frac{z+1}{2z}. \tag{13}$$

The disturbance transfer function is

$$Y^e(z) = \left.\frac{I_{dq}(z)}{-E^e(z)}\right|_{I_{dq}^{ref}=0} = \frac{W_L^e}{1 + W_L^e \cdot W_{REG}^e \cdot W_{FB}}. \tag{14}$$

Substituting (12), (13), (9) in (15), one gets

$$Y^e(z) = \frac{T_S \cdot e^{-j\omega_e T_S}}{L} \cdot \frac{z-1}{z^2 \cdot p_1 + z \cdot p_2 - e^{-\beta}(\alpha_d - 1)}, \tag{15}$$

$$p_1 = e^{-j\omega_e T_S} \quad , \quad p_2 = e^{-j\omega_e T_S}(\alpha_d - 1) - e^{-\beta},$$

which represents the disturbance transfer function of the closed-loop system in fundamental synchronous frame of reference.

When considering the stationary frame voltage disturbance at the frequency ω_x, and assuming that the synchronous d-q frame revolves at the speed ω_e, disturbance transfer function in stationary frame Y^s can be obtained from Y^e as

$$Y^s(z) = Y^s(e^{j\omega_x T_S}) = Y^e(e^{j\omega_x T_S} \cdot e^{-j\omega_e T_S})$$
$$= Y^e(e^{j(\omega_x - \omega_e)T_S}) = A(\omega_e, \omega_x) + j \cdot B(\omega_e, \omega_x). \tag{16}$$

Combining (15) with (16), setting ω_e to 314 rad/s and evaluating over the frequency band $f_x \in [-1000, 1000]$Hz disturbance transfer function, shown in Fig. 5, is obtained.
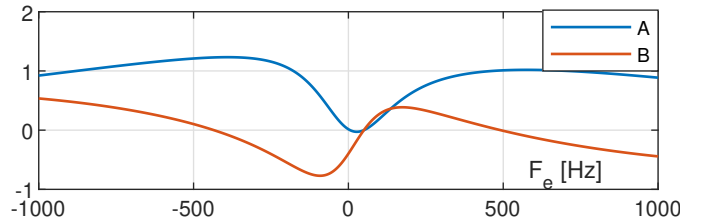

Fig. 5: Disturbance transfer function of closed-loop system shown in Fig. 2. The results are obtained with electrical frequency of 100Hz.
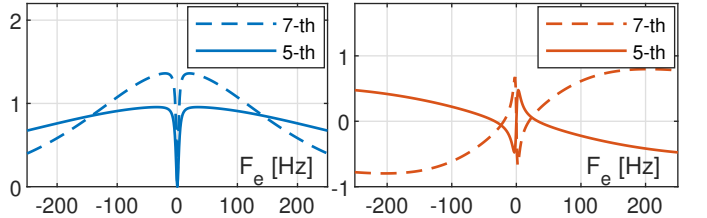

Fig. 6: Coefficients A (left) and B (right) for selected harmonics, over a range of fundamental frequencies.
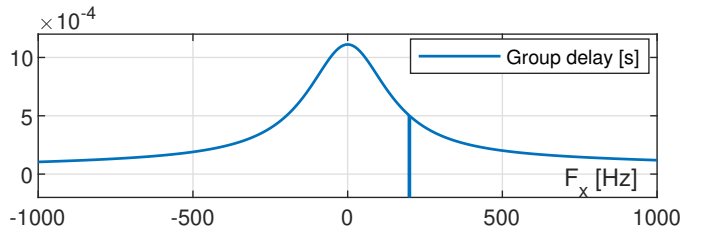

Fig. 7: Group delay of transfer function Y^s from (15), for $\omega_e = 314$ rad/s.

The stator current response to back-emf harmonics can be described by real part (A) and imaginary part (B) of the disturbance transfer function (16) for any disturbance frequency ω_x. While the curves in Fig. 5 provide $A(\omega_x)$ and $B(\omega_x)$ for the fixed fundamental frequency ω_e, the curves in Fig. 6 provide the change of $A(\omega_e, n)$ and $B(\omega_e, n)$ for n^{th} harmonic and variable excitation frequency ω_e. Transfer function of the equivalent load, W_{EQ}^n, for a nth harmonic regulator is

$$W_{EQ}^n = \frac{\overline{I_{dq}^n}}{U_{dq}^n} = A(\omega_e, n) + j \cdot B(\omega_e, n), \tag{17}$$

where $A(\omega_e, n)$ and $B(\omega_e, n)$ are coefficients obtained from (16) for a known electrical angular velocity, and for a chosen harmonic $n = 5, 7, 11, 13$ or higher.

Relation (17) calculates the output current harmonic response I_{dq}^n to the change of the voltage U_{dq}^n as a static relation. This approach is based on the fact that the dominant time constant of the disturbance transfer function $Y^e(z)$ is considerably shorter than the fundamental period. To support this claim, a consideration of the group delay introduced by $Y^e(z)$ dynamics is made. Group delay of transfer function $Y^e(z)$, obtained with $\omega_e = 50 \cdot 2 \cdot \pi$, is given in Fig. 7. Presumed step change of the 5th harmonic of input voltage would result in harmonic current response delayed by $\tau = 400 \mu s$ (Fig. 7). On these grounds, the group delay introduced by $Y^e(z)$ stands an order of magnitude lower than the sampling time of the harmonic controller up to the fundamental frequencies of 250Hz. If the fundamental frequency is larger, the impact of group delay becomes significant. The extent of such an impact is probed analytically and by means of computer simulations.

C. Design of Harmonic Controller

Each harmonic controller considers the feedback signals and derives the voltage command U_{dq}^n which is added to the main voltage reference U_{dq}, Fig. 2. The structure of the harmonic controller has to be based on the properties of the load (16), (17). Adopting internal model approach [12], the controller is designed by inverting the transfer function of the load and multiplying the outcome by an integrator and an adjustable gain α_n, where $n = 5, 7, 11, 13$ or higher, is the order of the considered harmonic:

$$W_{REG}^n(z) = W_{EQ}^n{}^{-1} \cdot \frac{\alpha_n \cdot z}{z-1} = \frac{A_n - j \cdot B_n}{A_n^2 + B_n^2} \cdot \frac{\alpha_n \cdot z}{z-1}, \quad (18)$$

where $A_n = A(\omega_e, n)$ and $B_n = A(\omega_e, n)$ depend on the fundamental frequency, as shown in Fig. 6. Structure of harmonic controller is given in Fig. 8. Closed-loop transfer function of the harmonic controller can be obtained by combining (18) and (17), and is given by

$$W_{CL}^n(z) = \frac{W_{REG}^n(z) \cdot W_{EQ}^n(z)}{1 + W_{REG}^n(z) \cdot W_{EQ}^n(z)} = \frac{z \cdot \alpha_n}{z \cdot (\alpha_n + 1) - 1}. \quad (19)$$

Transfer function (19) has only one root at $z_1 = (\alpha_n + 1)^{-1}$, which for $\alpha_n > 0$ is real and less than one. The correlation between s-domain and the z-domain poles is given by $z_1 = exp(s_1/f_e)$. Aforementioned real z-domain pole corresponds to the real s-domain pole which resides on the negative part of the real axis between $-\infty$ and 0. Parameter α_n will determine the settling time of the closed-loop harmonic suppression controller. closed-loop step response of the harmonic regulator is given in Fig. 9. Bode plot for a closed-loop 5th harmonic current controller for various values of parameter α_n is given in Fig. 10.

Whenever ω_e changes, parameters A_n and B_n need to be updated. This can be done by creating a look-up table derived from (16), or by means of an appropriate polynomial approximation. The use of the same gain α_n over the range of rotor speeds ensures the same closed-loop poles in z-domain. Yet, the s-domain poles and the time response will depend on the sampling time. Since the sampling time is equal to one period of the fundamental, the response will be considerably slower at low speeds. This does not seem to present a problem since, at the same time, the amplitude of harmonic disturbances increases with the speed, and they
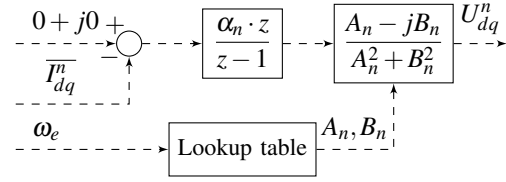

Fig. 8: The structure of nth the harmonic controller, for n^{th} harmonic, $n \in [5, 7, 11, 13]$ or higher.
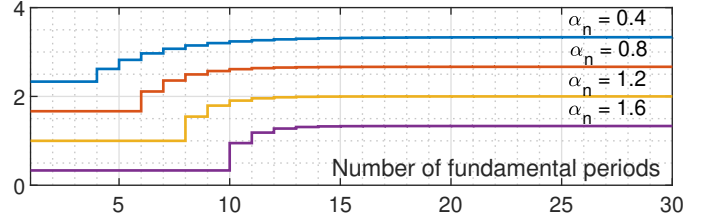

Fig. 9: Step response of the harmonic controller in closed loop, for various values of parameter α_n
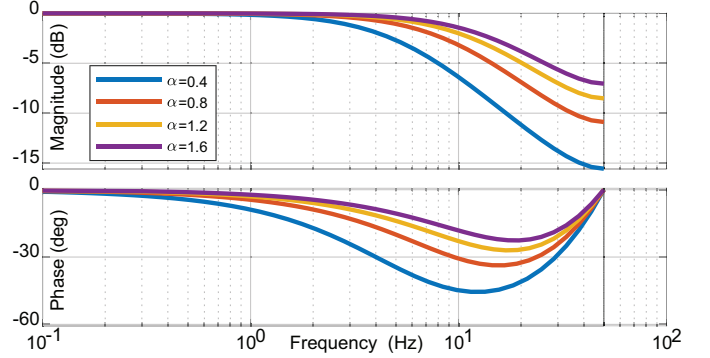

Fig. 10: Bode plot of closed-loop transfer function of (19) for various values of parameter α_n. The fundamental current frequency is $f_e = 100$Hz.
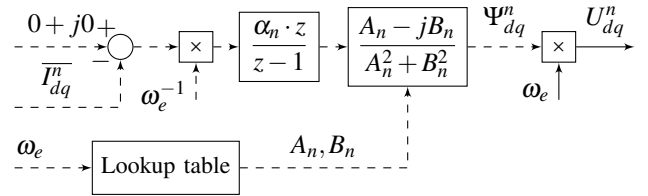

Fig. 11: Extension of controller structure from Fig. 8 for speed independent operation.

remain low at low rotor speeds. Moreover, at low rotor speeds and low frequencies of said harmonic disturbances, they fold back within the bandwidth of the standard digital current controller [27], which is fully capable of eliminating their impact on the output current.

The outputs of the harmonic regulator are the voltages U_d^n and U_q^n. At steady state, these voltages reach the values of corresponding back-emf harmonic disturbances. With back-emf harmonics neutralized by the corrective action of corresponding harmonic controllers, the stator current harmonics are equal to zero. However, if a fast enough change of speed occurs, the amplitude of harmonic disturbances would change in proportion with the speed, introducing a difference between the actual outputs of harmonic controllers and newly established disturbances. Thus, the current harmonics will arise for a few fundamental periods, and get compensated by the corrective action of the controller. The settling time of these transients is determined by the parameter α_n.

In order to eliminate the impact of sudden speed changes,

controller structure of Fig. 8 can be further enhanced. In order to achieve speed-independent operation, harmonic controllers can be restructured to output the ratio between the voltage command U_{dq}^n and the fundamental frequency ω_e, the signal which has dimension of the flux and which is intrinsically speed-independent. In the end, prior to adding all the voltage corrections of individual harmonic controllers to the main voltage reference, the flux-like voltage corrections are multiplied with ω_e to get the voltage command. Corresponding change of the structure of the harmonic controller is depicted in Fig. 11.

D. Dead-time Effects and their Compensation

Dead time is inserted in switching signals to prevent the short circuit of the dc link. Even though this time is very short, it causes distortion of the voltage waveforms, differences between the voltage commands and output voltages, and introduces current harmonics [28], [29], [30]. The voltage error caused by the dead time can be modeled as [30]

$$\Delta V_{a,b,c} = V_d \cdot sgn(I_{a,b,c}), \qquad (20)$$

where V_d represents the magnitude of the voltage error. Most implementations of the dead time are based on delaying the closure of the incoming switch by T_d, thus introducing an interval when none of the switches in one inverter leg conduct. The error magnitude V_d is proportional to T_d. The dead-time effects are also temperature dependent and load-current dependent [29] and they are difficult to model and compensate.

From [30], voltage errors ΔV_a, ΔV_b, ΔV_c can be transformed from three-phase to the two-phase stationary frame. Corresponding voltage errors can be split into harmonic components,

$$\begin{bmatrix} \Delta V_\alpha \\ \Delta V_\beta \end{bmatrix} = V_1 \cdot \begin{bmatrix} cos(\phi) + \frac{1}{5}cos(5\phi) - \frac{1}{7}cos(7\phi) - ... \\ sin(\phi) - \frac{1}{5}sin(5\phi) - \frac{1}{7}sin(7\phi) + ... \end{bmatrix}, \quad (21)$$

where $V_1 = 4 \cdot V_d/\pi$ and $\phi = \omega_e \cdot t$ represents the phase of the current vector. It can be seen that the dead-time errors produce odd voltage harmonics. These harmonics impact the phase currents, and their effect can thus be measured using the one-fundamental-averaging presented in this paper. They can then be compensated with harmonic regulators. Namely, the harmonic current controllers have the capability to suppress the back-emf induced disturbances, and they can also remove stator current harmonics caused by the dead-time effects. This is an inherent feature of the developed harmonic suppressor, since it is able to compensate the current harmonics regardless of what the cause of their existence is.

E. Parameter Setting

Transfer function of nth harmonic controller, from subsection III-C, is given in (18). Closed-loop transfer function of the harmonic controller is

$$W_{CC}^n = \frac{W_{REG}^n \cdot W_{EQ}^n}{1 + W_{REG}^n \cdot W_{EQ}^n} = \frac{\alpha_n \cdot z}{(1+\alpha_n)z-1}, \qquad (22)$$

where α_d is an adjustable parameter, which determines the closed-loop response. For probed values of α_n ranging from 0.2 to 2, the system is stable, and has no overshoots. For the purpose of the experiment, α_n is set to $\alpha_n = 0.8$, resulting in the closed-loop settling time of 3 sampling periods.

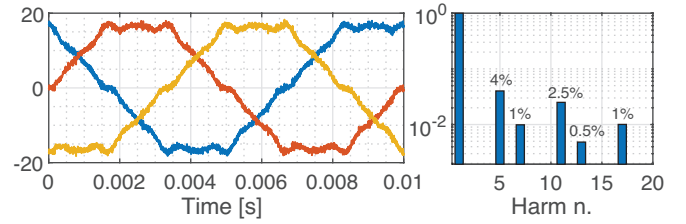**Fig. 12:** Waveforms of back-emf obtained as the open-circuit voltages from the laboratory prototype at $f_e = 100$Hz and corresponding spectrum (logarithmic scale).
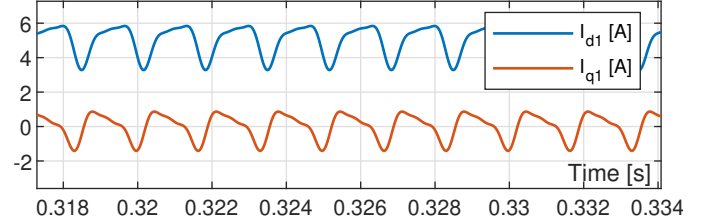

Fig. 13: Direct and quadrature current waveforms at electrical frequency of 100Hz.

IV. SIMULATION RESULTS

Proposed harmonic suppressing system, depicted in Fig. 4, is first verified by computer simulations. Harmonic content of non-sinusoidal back-emf of the motor is modelled according to actual measurements performed on a laboratory prototype, detailed in Appendix B, running with fundamental frequency of 100Hz. Corresponding waveforms are given in Fig. 12. Simulation model includes motor modelled as $R-L$ load with non-sinusoidal back-emf, PWM inverter with idealized power switches, and conventional digital current controller of [27]. In addition, the model is extended by the harmonic controller described in the previous section.

During simulations, d-axis and q-axis current references of the drive are set to

$$I_{dq}^{ref} = 4 + j \cdot 0. \qquad (23)$$

In operation with main digital current controller and without the harmonic controller, the waveforms of d-axis and q-axis currents are given in Fig. 13, with corresponding phase currents given in Fig. 14. It can bee seen from Fig. 14. that the conventional digital current controller of [27] does not suppress the current harmonics arising from the non-sinusoidal back-emf.

Before running the simulations of the whole system extended by the proposed harmonic controller, the structure and parameter setting of the harmonic controller have been verified, by checking the corresponding transient traces. With $\alpha_n = 0.7$ and with the harmonic controller enabled at $t = 0.56$s, the waveforms of Fig. 15 illustrate the suppression of the 5th, 7th and 11th harmonics. The waveforms prove that, once enabled, harmonic controller manages to suppress harmonic currents in 2-3 sampling periods.

As discussed in subsection II-B, sudden change of drive references I_d^{ref} and I_q^{ref} can introduce error into harmonic feedback signals, obtained by averaging the stator currents in corresponding reference frames for each harmonic. These effects introduce errors into harmonic suppression structure and deteriorate the final outcome. In Fig. 16 the waveforms of simulated d-axis and q-axis currents are shown with the har-
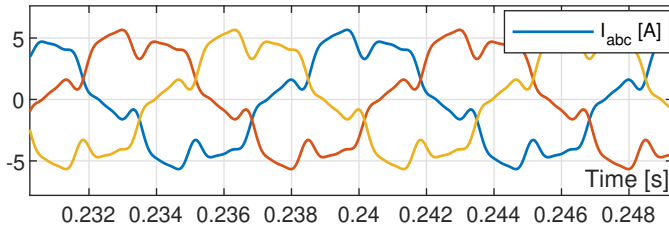
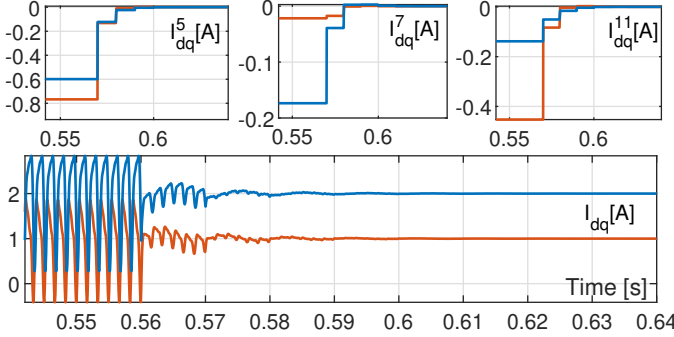**Fig. 14:** Phase currents obtained from simulation, with $f_e = 100$Hz, depicting severe harmonic distortion.

Fig. 15: Simulated waveforms of I_{dq} currents, showing the dynamic characteristic of harmonic controllers. At t = 0.56s harmonic controllers are enabled.
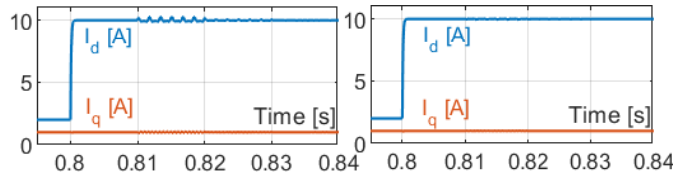

Fig. 16: Direct and quadrature currents step response in situation where the harmonic acquisition is (left) affected and (right) unaffected by the drive dynamics.
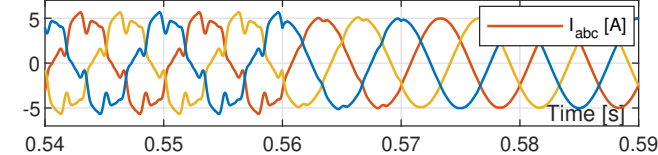

Fig. 17: Phase currents before and after harmonic compensation. Harmonic controllers are enabled at t = 0.56s.
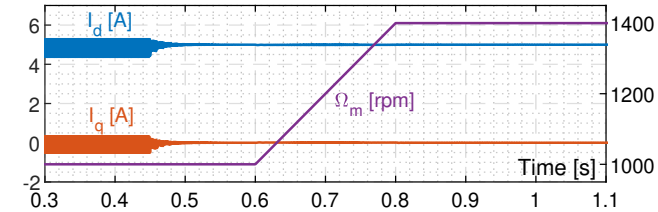

Fig. 18: The waveforms of direct and quadrature currents and the rotor speed obtained at the sudden speed ramp change. Harmonic controllers are enabled at t = 0.45s, and the machine experiences ramp speed change at t = 0.6s. Controller extension of Fig. 11 secures undisturbed operation with undistorted phase currents.

monic controllers enabled for $n \in [5, 7, 11, 13, 17]$ harmonics but without $\widehat{W}_{cc}^e(z)$ estimator introduced in Fig. 3. In these conditions, the step change of I_d^{ref} introduced at $t = 0.8$s produces considerable deterioration of the I_d waveform. Simulation is repeated with $\widehat{W}_{cc}^e(z)$ estimator enabled, and with the harmonic feedback extraction organized in accordance with Fig. 3. Now, the waveforms of I_d and I_q in Fig. 16 (b) are not affected by the I_{dq} steps, and the harmonic feedback acquisition proceeds undisturbed by the drive dynamics.
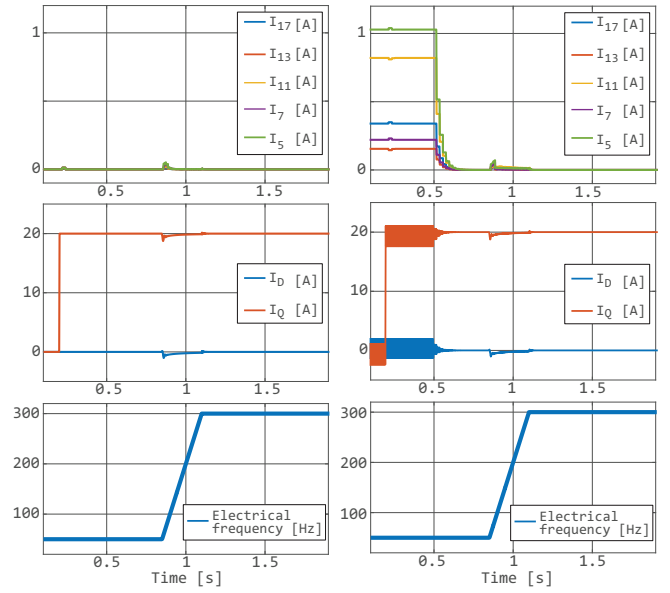
(a) Harmonic suppressor is disabled, and there is no harmonic content in the back-emf.

(b) Harmonic suppressor is enabled, and the machine has harmonic rich back-emf.

Fig. 19: The harmonic feedback path and I_{dq} currents during fast speed changes.
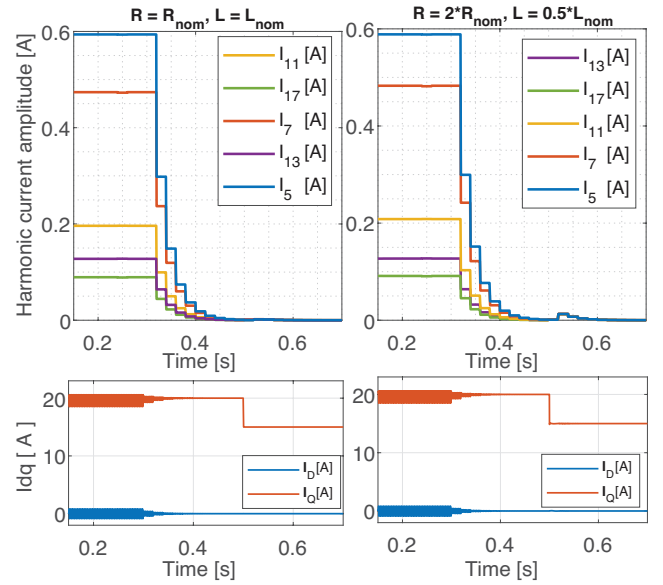

Fig. 20: Waveforms of harmonic currents (top) and I_{dq} currents (bottom) for nominal parameter setting (left) and erroneous parameter setting (right). Harmonic suppression is enabled at t = 0.3s, and a sudden step change of I_{dq}^{ref} occurs at t=0.5s.

Effectiveness of the presented solution is verified by simulating the drive with digital current controller of [12], with proposed harmonic compensation and with the feedback acquisition system of Fig. 3. In Fig. 17, the drive runs at $\omega_e = 628$rad/s , and the plots show the stator currents I_{abc}. Prior to $t = 0.56$s, harmonic controller is disabled, and the phase currents are distorted. At $t = 0.56$s, developed structure is enabled. In roughly two electrical periods, the impact of harmonic distortions is suppressed.

In order to verify the effectiveness of the controller extension of Fig. 11, suited to make the proposed suppressor robust against the changes in rotor speed and electrical frequency, the system is simulated while running at constant

speed with the suppressor enabled and experiencing a sudden, externally caused speed change (the second speed-controlled machine is used for this purpose; this is the reason for the average q-axis current to stay at zero). Corresponding waveforms of the stator direct and quadrature currents I_{dq} are given in Fig. 18 along with the change in the rotor speed. Simulation results obtained in Fig. 18 demonstrate that the controller extension of Fig. 11 provides robustness against the speed changes and secures firm harmonic suppression. Even when the drive experiences very high speed change rates ($\Delta f_e / \Delta t = 1000 Hz/s$) the harmonic suppression system experiences only a slight disturbance. When a very fast speed change occurs, initiated in the same manner in the simulation as explained in conjunction with Fig. 18, the fundamental controller experiences a brief disturbance, which cannot be predicted by the use of current estimator of (8), hence the disturbance in the harmonic feedback path. This is depicted in Fig. 19. Graphs of Fig. 19a show what effect a very fast speed change has on the harmonic feedback path when harmonic suppression is disabled, and there is no harmonic content in the back-emf, while Fig. 19b depicts the same scenario, but with harmonic rich back-emf and with harmonic suppression turned on.

Parameter sensitivity of the developed solution is investigated next, by studying the controller behaviour under large resistance and inductance variations. The results are given in Fig. 20 where traces of fundamental I_{dq} currents (bottom) and harmonic currents (top) are shown assuming correct parameter tuning (left) and erroneous parameter values (right). Increase of the resistance in the machine to 200% of the value used in the controllers (heavy duty operation with overload) and decrease of the inductance to half of the value used in the controllers (heavy saturation) are considered and results are shown for harmonic components up to the 17th, and for the fundamental. From these results it can be concluded that the current control scheme is very robust indeed since heavy detuning of parameters hardly affects the responses.

Finally, to show the effectiveness of harmonic current controllers in reducing the torque ripple, a simulation is done. Machine is modelled as an $R - L$ load, with harmonic rich back-emf. Back-emf harmonics which are simulated include 5th, 7th, 11th and 13th harmonic. The machine is kept operating at nominal electrical frequency f_e = 200Hz by an external speed-controlled load. Torque producing q-axis current reference is set to 50% of nominal value. Instantaneous, as well as average torque waveform, obtained by simulation, are shown in Fig. 21. Harmonic current controllers are initially inactive, and are enabled at $t = 0.4$s. A significant drop in the torque ripple is obvious. The residual torque ripple with the active harmonic current controllers enabled is due to interaction of phase current fundamental with back-emf harmonics.

V. EXPERIMENTAL RESULTS

Experimental verification is performed on a laboratory setup with a surface-mounted permanent magnet synchronous machine, hard-switched 3-phase PWM inverter and DSP-based programmable controller. The 8-pole BLDC motor has winding resistance of Rs = 0.1Ω, inductance $L = 100\mu$H, rated
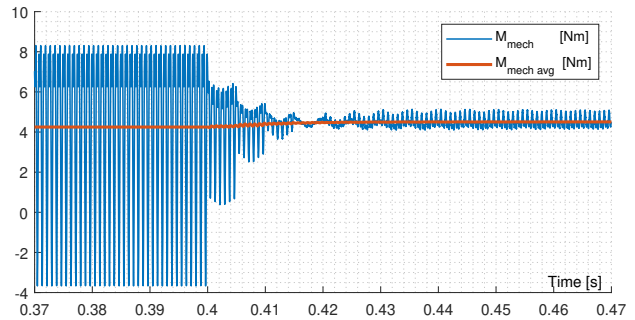

Fig. 21: Waveform of instantaneous (blue) and average (red) torque obtained by a simulation before and after harmonic compensation. Machine is operating at $f_e = 200$Hz, with phase currents amplitude $I_{phase} = 0.5 \cdot I_{nom}$. Harmonic current controllers are enabled at $t = 0.4$s. Drastic reduction of torque ripple is evident.

frequency of 200Hz and rated current of $I_{rated} = 25$A. The machine is fed from a PWM inverter with $f_{pwm} = 40$kHz, minimum dead time of $T_d = 160$ns, and with $V_{DC} = 72$V. The experimental setup has been developed for powering a small electrical vehicle. Experimental waveforms of non-sinusoidal back-emf obtained by measuring open-circuit voltages at $f_e = 100$Hz are given in Fig. 12. To synthesize the harmonic current controller, the transfer function of the equivalent load (17) of the current controlled machine has to be known. The coefficients $A_n(\omega_e, n)$ and $B_n(\omega_e, n)$ of (17) can be calculated in real time, since they are unambiguously defined for a targeted harmonic number n at operating angular frequency ω_e. The look-up table is however implemented instead in the experimental setup, because of the faster execution time (as the calculations can be done offline; however, as noted, direct calculation in real time is also possible at the expense of a longer execution time). The implementation of the look-up table is rather simple; pre-calculated values of A_n and B_n for a targeted harmonic are stored in an array with sufficient quantization density in regards to ω_e.

The waveforms of Fig. 22 represent the phase current along with the corresponding spectrum obtained at the rotor speed of Ω_{meh} = 1500 rpm, where the fundamental frequency is 100Hz. The dead time is set to its rated value of 160ns while the harmonic suppressor is disabled. Due to the back-emf harmonics and dead-time effects, the phase currents are distorted considerably. The waveforms of Fig. 23 represent the phase current along with the corresponding spectrum obtained at same speed of $n = 1500$rpm with the novel harmonic suppressor fully enabled. Compared to Fig. 22, the relevant current harmonics are reduced more than 100 times. Residual value are mainly caused by the noise and quantization effects within the feedback chain. Total harmonic distortion is reduced from 25.25% down to 0.48%. Results of Fig. 22 and Fig. 23 demonstrate the steady state operation of the system with the nominal dead time of 160ns.

In order to check dynamic performance, Fig. 24 illustrates transient waveforms obtained upon turning on the harmonic suppressor, which prove that the presented solution reduces the q-axis current ripple from 1.525A down to 0.211A, keeping the ripple below 0.8% of the rated current. Thus, reduction of the q-axis current ripple does not follow reported reduction of the total harmonic distortion (Fig. 23) and the residual q-axis
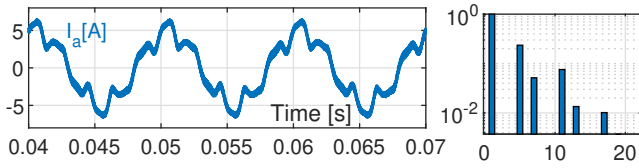
Fig. 22: The waveform and spectrum of the phase current obtained at 1500 rpm without the novel harmonic suppressor.
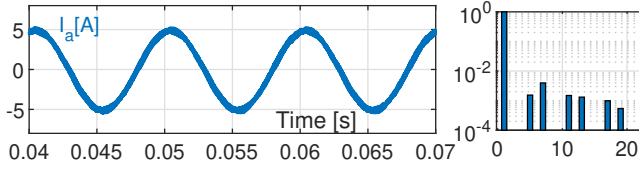

Fig. 23: The waveform and spectrum of the phase current obtained at 1500 rpm with the proposed harmonic suppressor.
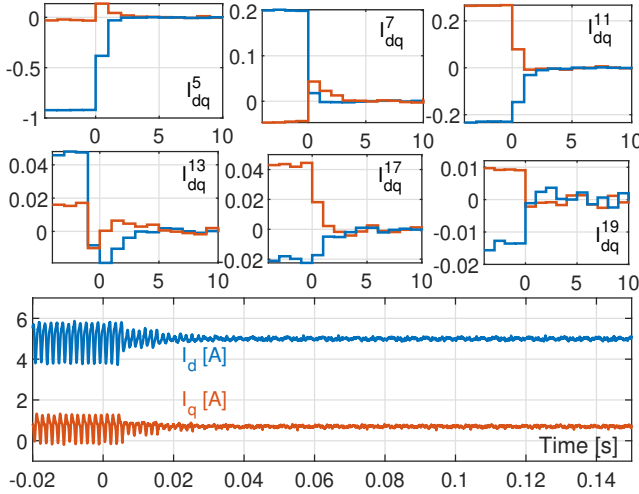

Fig. 24: Transient waveforms obtained upon turning on the proposed harmonic suppressor. The waveforms are obtained at 1500rpm and with rated dead time of 160 ns. The harmonic suppressor is turned on at t = 0.005s. The plots (top left - center right) depict the harmonic feedback obtained in the corresponding reference frame for the six most relevant harmonics. The waveform (bottom) represents the d-axis and q-axis current components.

current ripple comprises components that are not related to the back-emf harmonics and the dead time.

In order to prove that the step changes of the drive current references I_{dq}^{ref} do not disturb the harmonic suppressor, the d-axis and q-axis currents are measured with the harmonic suppressor enabled and with the drive current references exhibiting step change. Experimental waveforms are given in Fig. 25. The traces of Fig. 25 (left) prove that the I_{dq}^{ref} step introduces disturbances into the feedback acquisition and results in visible disturbances of d-axis and q-axis currents. The undisturbed waveforms shown in Fig. 25 (right) correspond to the case where the current estimator is applied according to Fig. 3.

In order to verify the capability of the solution to suppress the harmonic currents caused by the dead time, the dead time is intentionally increased to 5% of the PWM period. Corresponding waveforms of the phase currents are given in Fig. 26, without the harmonic suppressor (left) and with the harmonic suppressor (right). Improvement in the operation is evident, although the control system does not include a conventional dead-time compensator.

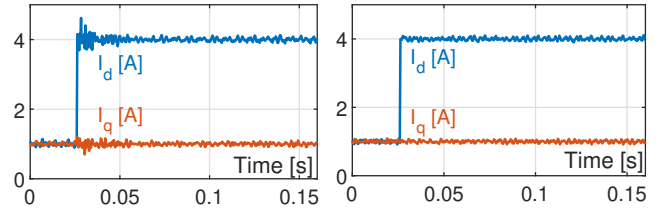The results of a test conducted at fundamental frequency

Fig. 25: Experimental waveforms of d-axis and q-axis currents obtained with I_{dq}^{ref} steps and with the proposed harmonic suppressor enabled. Traces (left) are obtained without the estimator $W_{cc}(z)$ of Fig. 3, while traces (right) show that the use of the structure of Fig. 3 effectively removes corresponding disturbances.
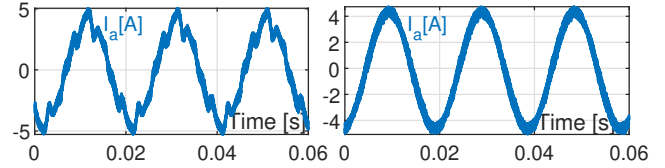

Fig. 26: Experimental waveforms of the phase currents obtained with an increased dead time of 5%. The waveform (left) is obtained without the harmonic suppressor. The waveform (right) is obtained with the developed harmonic suppressor enabled.
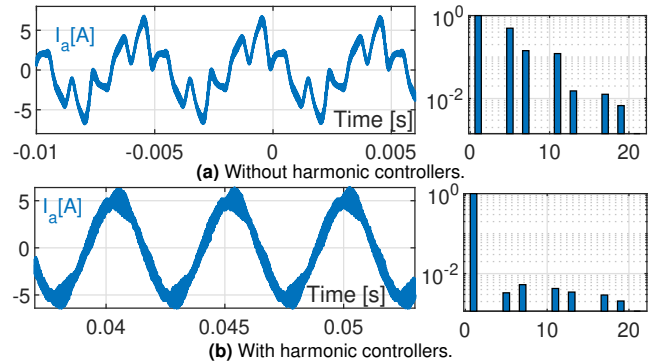

(a) Without harmonic controllers.

(b) With harmonic controllers.

Fig. 27: Phase currents and respective harmonic content with and without harmonic controllers, at $f_e = 200$Hz.

of 200Hz are shown in Fig. 27. At 200Hz, the THD without the harmonic suppressor reaches 53.11%, while THD with the suppressor is below 0.91%.

Regarding the computational resources needed to implement the proposed harmonic suppression system in a DSP, the execution times were measured. The execution time of fundamental current regulator, with standard protection and monitoring functions, is measured to be 3.5μs. After enabling the harmonic current controllers, for up to the 19th harmonic, the execution time increases to a total of 5μs. It is important to note that this increase in execution time does not affect the latency of fundamental current controller, as the harmonic suppressor algorithm can be executed after updating the PWM compare registers.

In order to prove the capability of the proposed controller to suppress the torque ripple, one has to use a fast and accurate torque transducer with the bandwidth beyond 1 kHz, which was not available. Hence, to circumvent this problem, an indirect proof is provided. Differences in the torque ripple resulting with and without harmonic suppressor are assessed, by measuring the vibration of the machine housing and fixtures using a vibrometer. The results of the test are depicted in Fig. 28. Machine is rotating at 1800rpm which corresponds to electrical frequency of f_e=100Hz. The results in Fig. 28 show -40dB reduction in vibration power at the sixth harmonic
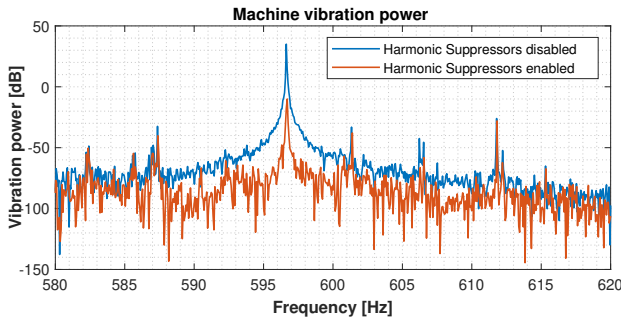
Fig. 28: Zoomed-in view of the machine vibration spectrum. The component at 596Hz shows drastic reduction of the 6th harmonic of electromagnetic torque once the harmonic suppression system is enabled.

f_e [Hz]	P_{in}^{off} [W]	P_{in}^{on} [W]	$\Delta P_{in}/P_{in}^{off}$ [%]
50	14.845	14.565	1.8862
75	24.360	23.240	4.5977
100	34.612	33.320	3.7328
125	44.988	43.900	2.4184

TABLE I: Input power before and after enabling the harmonic suppressor.

frequency once the harmonic suppression system is enabled, which implies significant reduction of the 5th and 7th harmonic currents generated torque ripple. Similar findings are obtained with key remaining harmonics. To further support this claim, the differences in input power for a machine with constant fundamental current amplitude are given in Table I, before and after enabling the harmonic suppressor.

VI. CONCLUSION

Permanent magnet dc motors are widely used both in high-volume applications such as electrical vehicles and in high-performance applications such as the industrial drives. The need to increase specific torque, reduce the volume and weight, and produce the motors with less active materials usually results in electrical machines with non-sinusoidal electromotive forces that give rise to current harmonics and the torque ripple.

Another source of the phase current harmonics and the torque ripple is the PWM inverter dead time. Whenever the drive runs at speeds commensurate to the rated speed, the frequency of corresponding phase current harmonics is well beyond the closed-loop bandwidth of conventional digital current controllers and cannot be compensated.

In this paper, a novel harmonic suppressor is presented as an extension of the conventional digital current controller. The uniqueness of presented solution is theoretically infinite suppression of each individual current harmonic. In practice, the suppression is defined by one low significant bit (LSB) of ADC. Most importantly, the harmonic suppression system does not affect the main current loop dynamics.

Simulations and experimental results prove the method to be successful, both in steady state conditions and in transients. Whether running at high or low speeds, activation of the proposed harmonic controller effectively suppresses the stator current harmonics in just 2-3 periods of the fundamental waveform. Reduction of the stator current total harmonic distortion by more than 50 times is experimentally proved both at the rated speed and at one half of the rated speed. By considering the q-axis current waveforms, the torque ripple from all the

sources is reduced more than 7 times and maintained below 1% even with the motor with considerable distortion of the back-emf.

The developed method can be applied to any three-phase or multiphase (more than three phases) AC machine, and can be used either as just a dead-time compensator or — as the case is in this paper — a compensator of current harmonics produced simultaneously by multiple sources.

The solution developed and presented in this paper is at this point in time the only one that enables practically complete suppression of harmonic currents in the analysed drive system. However, this does not mean that other approaches cannot achieve the same or at least similar results. Hence the intention is to investigate in future work applicability and performance of repetitive control, dead-beat control, and PR control in the context of the same problem, and perform subsequently a comparative analysis of pros and cons of different solutions.

APPENDIX A - TRANSFER FUNCTIONS

The experimental setup runs with the sample time $T_s = 2\,T_{PWM}$. The control interrupt which acquires and processes the feedback, executes the controller and reloads the PWM compare registers, completes just before the next PWM period. Thus, the current $i^s = i_\alpha + j \cdot i_\beta$ in stationary $\alpha\beta$ reference frame [27] changes according to

$$i_{n+1}^s = i_n^s \cdot e^{-\beta} + u_n^s \cdot (1 - e^{-\beta})/R, \qquad (24)$$

where $\beta = RT_s/L$. With $i^s = i^e \cdot e^{j\theta_e}$, $u^s = u^e \cdot e^{j\theta_e}$ and with $\theta_e^{n+1} \approx \theta_e^n + \omega_e T_s$, current in the SRF is

$$i_{n+1}^e \cdot e^{+j\omega_e T_s} = i_n^e \cdot e^{-\beta} + u_n^e \cdot T_s/L. \qquad (25)$$

From (25), and with $(1 - e^{-\beta})/R \approx T_s/L$,

$$(ze^{+j\omega_e T_s} - e^{-\beta})I^e(z) = \frac{T_s}{L} \cdot U^e(z), \qquad (26)$$

$$W_L^e = \frac{I_{dq}(z)}{U^e(z)}\bigg|_{E_{\alpha\beta}=0} = \frac{T_s}{L}\frac{1}{ze^{j\omega_e T_s} - e^{-\beta}}. \qquad (27)$$

The feedback is obtained by one-period averaging [27], modelled by

$$W_{FB}(z) = \frac{I_{dq}^{FB}(z)}{I_{dq}(z)} = \frac{z+1}{2z}. \qquad (28)$$

With controller design constrained by casuality, one has

$$W_{REG}^e(z) = \frac{\alpha z}{z-1} \cdot (W_L^e(z))^{-1} \cdot \frac{1}{z}, \qquad (29)$$

$$W_{OL}^e(z) = W_L \cdot W_{REG} = \frac{\alpha}{z-1}, \qquad (30)$$

while the closed-loop transfer function is

$$W_{CC}^e = \frac{I_{dq}}{I_{dq}^{ref}} = \frac{W_{OL}^e}{1 + W_{OL}^e \cdot W_{FB}} = \frac{2 \cdot \alpha_d \cdot z}{2 \cdot z^2 + (\alpha_d - 2) \cdot z + \alpha_d}. \qquad (31)$$

APPENDIX B - EXPERIMENTAL SETUP PARAMETERS

Motor type	Permanent magnet SM
Number of poles	2p = 8
Motor rated current:	I_{rated} = 24 A_{rms}
Rated electrical frequency:	f_{rated} = 200Hz
Back-EMF constant:	k_e = 0.0255 V_{Peak} / (rad/s)
Stator resistance:	R_s = 0.1 Ω
Stator inductance:	L_s = (L_d + L_q)/2 = 100 μH
DC-bus voltage:	V_{DC} = 72 V
PWM frequency:	f_{PWM} = 1 / T_{PWM} = 40 kHz
Regulation frequency:	f_s = 1 / T_s = 20 kHz

Rated dead time:	T_d = 160 ns
ADC resolution:	N_{ADC} = 12bit
Oversampling period:	T_{ADC} = T_{PWM} / 32
PWM method:	Symmetrical PWM
DSP controller:	TMS320F28379D

REFERENCES

[1] T. Sheng, X. Wang, J. Zhang, and Z. Deng, "Torque-ripple mitigation for brushless dc machine drive system using one-cycle average torque control," *IEEE Trans. Ind. Electron.*, vol. 62, no. 4, pp. 2114–2122, 2015.

[2] Z. Q. Zhu and D. Howe, "Electrical machines and drives for electric, hybrid, and fuel cell vehicles," *Proceedings of the IEEE*, vol. 95, no. 4, pp. 746–765, 2007.

[3] C. Xia, G. Jiang, W. Chen, and T. Shi, "Switching-gain adaptation current control for brushless dc motors," *IEEE Trans. Ind. Electron.*, vol. 63, no. 4, pp. 2044–2052, 2016.

[4] M. Sumega, S. Zossak, P. Varecha, and P. Rafajdus, "Sources of torque ripple and their influence in BLDC motor drives," *Transportation Research Procedia*, vol. 40, pp. 519 – 526, 2019.

[5] X. Li, G. Jiang, W. Chen, T. Shi, G. Zhang, and Q. Geng, "Commutation torque ripple suppression strategy of brushless dc motor considering back electromotive force variation," *Energies*, vol. 12, no. 10, p. 1932, 2019.

[6] W. Chen, Y. Liu, X. Li, T. Shi, and C. Xia, "A novel method of reducing commutation torque ripple for brushless dc motor based on cuk converter," *IEEE Trans. Power Electron.*, vol. 32, no. 7, pp. 5497–5508, 2017.

[7] R. K. Achary, S. Durgaprasanth, C. Nagamani, and G. S. Ilango, "A simple voltage modulator scheme for torque ripple minimization in a permanent magnet brushless dc motor," *IEEE Trans. Power Electron.*, vol. 35, no. 3, pp. 2809–2818, 2020.

[8] X. Li, C. Xia, Y. Cao, W. Chen, and T. Shi, "Commutation torque ripple reduction strategy of z-source inverter fed brushless dc motor," *IEEE Trans. Power Electron.*, vol. 31, no. 11, pp. 7677–7690, 2016.

[9] M. P. Maharajan and S. A. E. Xavier, "Design of speed control and reduction of torque ripple factor in bldc motor using spider based controller," *IEEE Trans. Power Electron.*, vol. 34, no. 8, 2019.

[10] S. Noguchi, K. Suzuki, and H. Dohmeki, "The efficiency comparison by exciting waveform of the square-wave brushless dc motor," in *18th Int. Conf. on Electrical Machines and Systems (ICEMS)*, 2015.

[11] M. Bertoluzzo, G. Buja, R. K. Keshri, and R. Menis, "Sinusoidal versus square-wave current supply of pm brushless dc drives: A convenience analysis," *IEEE Trans. on Ind. Electron.*, vol. 62, no. 12, pp. 7339–7349, 2015.

[12] S. N. Vukosavic, *Grid-Side Converters Control and Design*. Springer, Switzerland, 2018.

[13] S. N. Vukosavic, L. S. Peric, and E. Levi, "Digital current controller with error-free feedback acquisition and active resistance," *IEEE Trans. Ind. Electron.*, vol. 65, no. 3, pp. 1980–1990, 2018.

[14] J. R. Hendershot and T. J. E. Miller, *Design of brushless permanent-magnet motors*. Magna Physics Pub; Clarendon Press Hillsboro, OH: Oxford, 2010.

[15] H. Dhulipati, S. Mukundan, C. Lai, K. Mukherjee, J. Tjong, and N. C. Kar, "Multiple reference frame-based extended concentrated wound PMSM model considering PM flux linkage and inductance harmonics," *IEEE Trans. Energy Convers.*, vol. 34, no. 2, pp. 731–740, 2019.

[16] P. Mattavelli, L. Tubiana, and M. Zigliotto, "Torque-ripple reduction in PM synchronous motor drives using repetitive current control," *IEEE Trans. Power Electron.*, vol. 20, no. 6, pp. 1423–1431, 2005.

[17] M. Tang, A. Gaeta, A. Formentini, and P. Zanchetta, "A fractional delay variable frequency repetitive control for torque ripple reduction in PMSMs," *IEEE Trans. Ind. Appl.*, vol. 53, no. 6, pp. 5553–5562, 2017.

[18] M. Tang, A. Formentini, S. A. Odhano, and P. Zanchetta, "Torque ripple reduction of PMSMs using a novel angle-based repetitive observer," *IEEE Trans. Ind. Electron.*, vol. 67, no. 4, pp. 2689–2699, 2020.

[19] G. Feng, C. Lai, and N. C. Kar, "A closed-loop fuzzy-logic-based current controller for PMSM torque ripple minimization using the magnitude of speed harmonic as the feedback control signal," *IEEE Trans. Ind. Electron.*, vol. 64, no. 4, pp. 2642–2653, 2017.

[20] C. Lai, G. Feng, K. L. V. Iyer, K. Mukherjee, and N. C. Kar, "Genetic algorithm-based current optimization for torque ripple reduction of interior PMSMs," *IEEE Trans. Ind. Applicat.*, vol. 53, no. 5, pp. 4493–4503, 2017.

[21] J. Liu, H. Li, and Y. Deng, "Torque ripple minimization of PMSM based on robust ilc via adaptive sliding mode control," *IEEE Trans. Power Electron.*, vol. 33, no. 4, pp. 3655–3671, 2018.

[22] W. Qian, S. Panda, and J.-X. Xu, "Torque ripple minimization in PM synchronous motors using iterative learning control," *IEEE Trans. Power Electron.*, vol. 19, no. 2, pp. 272–279, 2004.

[23] G. Feng, C. Lai, J. Tian, and N. C. Kar, "Multiple reference frame based torque ripple minimization for PMSM drive under both steady-state and transient conditions," *IEEE Trans. Power Electron.*, vol. 34, no. 7, pp. 6685–6696, 2019.

[24] G. Feng, C. Lai, X. Tan, B. Wang, and N. C. Kar, "Optimal current modeling and identification for fast and efficient torque ripple minimization of PMSM using theoretical and experimental models," *IEEE Trans. Ind. Electron.*, vol. 68, no. 12, pp. 11 806–11 816, 2021.

[25] K. Nakamura, H. Fujimoto, and M. Fujitsuna, "Torque ripple suppression control for PM motor with high bandwidth torque meter," in *2009 IEEE Energy Conversion Congress and Exposition*, 2009, pp. 2572–2577.

[26] S. N. Vukosavic, L. S. Peric, and E. Levi, "Ac current controller with error-free feedback acquisition system," *IEEE Trans. Energy Convers.*, vol. 31, no. 1, pp. 381–391, 2016.

[27] S. N. Vukosavic, L. S. Peric, and E. Levi, "A three-phase digital current controller with improved performance indices," *IEEE Trans. Energy Convers.*, vol. 32, no. 1, pp. 184–193, 2017.

[28] Y. Ji, Y. Yang, J. Zhou, H. Ding, X. Guo, and S. Padmanaban, "Control strategies of mitigating dead-time effect on power converters: An overview," *Electronics*, vol. 8, no. 2, p. 196, Feb 2019.

[29] Y. Yang, K. Zhou, H. Wang, and F. Blaabjerg, "Analysis and mitigation of dead-time harmonics in the single-phase full-bridge PWM converter with repetitive controllers," *IEEE Trans. Ind Appl.*, vol. 54, no. 5, 2018.

[30] S. Kim and S. Park, "Compensation of dead-time effects based on adaptive harmonic filtering in the vector-controlled ac motor drives," *IEEE Trans. Ind. Electron.*, vol. 54, no. 3, 2007.

Miodrag G. Joksimovic (S'18) was born in Cetinje, Yugoslavia, in 1995. He received BSc and MSc degrees from the University of Belgrade, Belgrade, Serbia in 2019 and 2020, respectively, all in Electrical Engineering. In 2019 he was head of software development at H-Bridges, a first prized student team competing at IEEE International Future Energy Challenge. His research interests are focused on digital control of electrical drives and gridside converters, and power conversion in renewable energy sources.

Emil Levi (S'89, M'92, SM'99, F'09) received his MSc and the PhD degrees in Electrical Engineering from the University of Belgrade, Yugoslavia in 1986 and 1990, respectively. He joined Liverpool John Moores University, UK in May 1992 and is since September 2000 Professor of Electric Machines and Drives. He served as a Co-Editor-in-Chief of the IEEE Trans. on Industrial Electronics in the 2009-2013 period. Currently he is Editor-in-Chief of the IEEE Trans. on Industrial Electronics and Editor-in-Chief of the IET Electric Power Applications. He is the recipient of the Cyril Veinott award of the IEEE Power and Energy Society for 2009 and the Best Paper award of the IEEE Trans. on Industrial Electronics for 2008. In 2014 he received the "Outstanding Achievement Award" from the European Power Electronics (EPE) Association and in 2018 the "Professor Istvan Nagy Award" from the Power Electronics and Motion Control (PEMC) Council.

Slobodan N. Vukosavic (M'93, SM'12) was born in Sarajevo, Yugoslavia, in 1962. He received the B.S., M.S., and Ph.D. degrees from the University of Belgrade, Belgrade, Yugoslavia, in 1985, 1987, and 1989, respectively, all in Electrical Engineering. He was with the Nikola Tesla Institute, Belgrade, Yugoslavia, until 1988, when he joined the ESCD Laboratory of Emerson Electric, St. Louis, MO. Since 1991, he worked with Vickers Electric Company and MOOG Electric. S.N. Vukosavic is with the Department of Electrical Engineering, The University of Belgrade, and Serbian Academy of Sciences and Arts. His interests include digital control, power conversion in renewable energy sources and power quality. He has published over 100 papers, 4 textbooks and 7 monographs and has completed over 42 large R/D and industrial projects.